

Construction of Defect-Engineered Three-Dimensionally Ordered Macroporous WO₃ for Efficient Photocatalytic Water Oxidation Reaction

Yating Wang^{*,a}, Chaosheng Peng^a, Tao Jiang^a, Jing Zhang^c, Zheng Jiang^d, and

Xingang Li^{*,b}

^a*Tianjin Key Laboratory of Brine Chemical Engineering and Resource Eco-utilization, School of Chemical Engineering and Material Science, Tianjin University of Science & Technology, Tianjin 300457, P. R. China.*

^b*Collaborative Innovation Center of Chemical Science and Engineering (Tianjin), Tianjin Key Laboratory of Applied Catalysis Science & Engineering, School of Chemical Engineering & Technology, Tianjin University, Tianjin 300072, P. R. China.*

^c*Beijing Synchrotron Radiation Facility, Institute of High Energy Physics, Chinese Academy of Sciences, Beijing 100049, P. R. China.*

^d*Shanghai Synchrotron Radiation Facility, Shanghai Institute of Applied Physics, Chinese Academy of Sciences, Shanghai 201800, P. R. China.*

*Corresponding author

Email: wangyating@tust.edu.cn

xingang_li@tju.edu.cn

1. Experimental section

1.1 Material characterizations

The X-ray diffraction (XRD) pattern was detected with a Power X-ray diffractometer (Panalytical B.V., The Netherlands). The excitation light source was Cu K α ($\lambda = 1.5418$ Å), the scanning range of 2θ was from 20° to 80° and the scanning rate is 8°min^{-1} .

Thermogravimetric analysis (TG) experiment was performed on a Hitachi STA7300 compositional analysis instrument (GAA-0748) from 30 to 900°C under air atmosphere at a heating rate of $10^\circ\text{C}\cdot\text{min}^{-1}$.

Scanning electron microscopy (SEM) images were performed on a field emission scanning electron microscope (S-4800, Hitachi, Japan). Transmission electron microscopy (TEM) images were gained through a transmission electron microscope equipment (Japan JEOL, JEM-2100F), so do the energy dispersive X-ray spectroscopy (EDS) mode, relational EDS line-scanning and element mapping.

The specific surface areas and pore volume of samples were determined through nitrogen adsorption-desorption isotherms at -196°C collected on a Quantachrome QuadraSorb SI gas adsorption analyzer.

Ultraviolet-visible diffuse reflectance spectra (UV-Vis DRS) were detected by a spectrophotometer (Lambda750S, PerkinElmer, America). Raman spectra were tested by using the Raman system (InVia Reflex, Renishaw, England). The excitation wavelengths of light source were 325 and 532 nm.

X-ray photoelectron spectra (XPS) was detected by XPS system (ESCALAB 250Xi, Thermo Fisher Scientific Inc, USA).

Electron paramagnetic resonance (EPR) was measured on an electro paramagnetic resonance spectrometer (A300, Bruker, Germany) in liquid nitrogen.

Photoluminescence spectra (PL) were received on a fluorescence spectrophotometer (Fluorolog-3, Horiba Jobin Yvon Inc., Japan) under normal temperature conditions.

The extended X-ray absorption fine structure (EXAFS) spectroscopy measurements were operated in transmission mode on beamline BL14W1 (Shanghai Synchrotron Radiation Facility, China) and beamline 1W1B (Beijing Synchrotron Radiation

Facility, China) at nature temperature, 250 mA, 3.5 GeV.

The ultraviolet photoelectron spectra (UPS) were collected using the Thermo ESCALAB 250Xi PHI5000 VersaProbe III with He I radiation ($h\nu = 21.22$ eV). The pass energy is 1.3 eV and step size is 0.04 eV. Fermi energy (E_{FE}) of sample was calculated according to the equation:

$$E_{FE} = h\nu - E_{cutoff}$$

in which $h\nu$ is 21.22 eV, E_{cutoff} is the onset of the secondary emission[1, 2].

The turnover number (TON) and turnover frequency (TOF) can be defined by the following equation[3, 4]:

$$TON = \frac{\text{number of reacted holes}}{\text{number of active sites}}$$
$$TOF = \frac{\text{number of reacted holes}}{\text{number of active sites} \times \text{reaction time}}$$

Determining the number of an active site for a photocatalyst is often difficult; therefore, the number of reacted holes to the total number of WO_3 photocatalyst was used as a turnover number. The turnover number and turnover frequency obtained by this procedure is smaller than the actual turnover number.

In addition, The apparent quantum yields (AQE) of photocatalytic O_2 production could evaluate the photocatalytic activity of prepared photocatalyst using the same experimental setup as photocatalytic oxygen evolution measurements, except for the addition of a 400 nm band pass filter. The AQE was estimated as the following equation:

$$AQE(\%) = \frac{\text{Number of reacted holes}}{\text{Number of incident photons}} \times 100 = \frac{4MN_Ahc}{AIt\lambda} \times 100$$

where M , N_A , h and c represent the number of oxygen molecules, Avogadro's constant, Planck constant and light velocity, respectively. The total number of incident photons was measured using a PM100D power meter. A is the irradiation area (36.3 cm^2), t is the reaction time (1 h) and λ is the wavelength of light (400 nm).

1.2 Photoelectrochemical measurements

The photoelectrochemical properties were determined by a standard three-electrode electrochemical configuration (Chenhua, China) in 100 mL 1M KOH (PH = 14)

electrolyte at 25 °C under simulated solar light illumination. Pt electrode and Ag/AgCl electrode were used as a counter electrode and a reference electrode, respectively. The working electrode was prepared by drop-coating samples over the fluorine-doped tin oxide (FTO) glass substrate. Generally, 400 μ L distilled water, 100 μ L absolute ethanol, 40 mg samples and 3 μ L Nafion ionomer as adhesive with ultrasonic stirring to form a homogenous ink. Then the FTO glass substrate was covered with a thin layer of uniform film by dropping 4 μ L ink onto it by a micro-syringe with an exposed surface area of about 1 \times 1 cm. The photoelectrochemical experiments were conducted in a CHI 640E electrochemical analysis station (Chenhua, China) under simulated solar light illumination. Mott-Schottky plots were measured at a frequency of 1000 Hz with a bias potential ranging from 1.0 V to -1.0 V (vs. Ag/AgCl). Chronoamperometry tests were conducted at 0.5 V. Electrochemical impedance spectra (EIS) were conducted in the frequency from 1 mHz to 0.1 MHz.

We also used the electrochemical Mott-Schottky method to measure the flat band potential (E_{fb}) of W270-400 at 500Hz, 800 Hz, 1000 Hz and 1200 Hz, as shown in Figure S1. The almost coincident curves and similar intercept at different frequency eliminate the frequency dispersion. Thus, we set the frequency of electrochemical Mott-Schottky method as 1000 Hz to calculate the measure the flat band potential (E_{fb}) vs NHE.

1.3 Optimization of calcination temperature

We have measured the TG-DTA of PS spheres template to determine the calcination temperature. As shown in Figure S2A, the weight loss of PS270 is close to 100 % at 500°C. Thus, we tried to prepare 3DOM WO₃ at 500 °C, 600 °C and 700 °C, and found that calcination temperature over 500 °C will cause particle sintering and structural collapse, as shown in Figure S3. In order to obtain a sample of tungsten trioxide with three-dimensional ordered macroporous structure and good crystallinity, 500 °C was selected as the calcination temperature, and the PS spheres template was removed at this temperature to obtain three-dimensional ordered samples with different pore

diameters.

1.4 Optimization of thermal-treating atmospheres

We optimized the reduction atmospheres for 0%, 8%, 20%, 50% and 100% H₂ in N₂ during the thermal treatment of WO₃ in our previous research[5]. We found the photocatalytic activity of thermal-treated WO₃ in 20% H₂ in N₂ was highest among the samples thermal-treated in different atmospheres. Thus, we set the thermal-treating atmospheres as 20% H₂ in N₂.

2. Figures

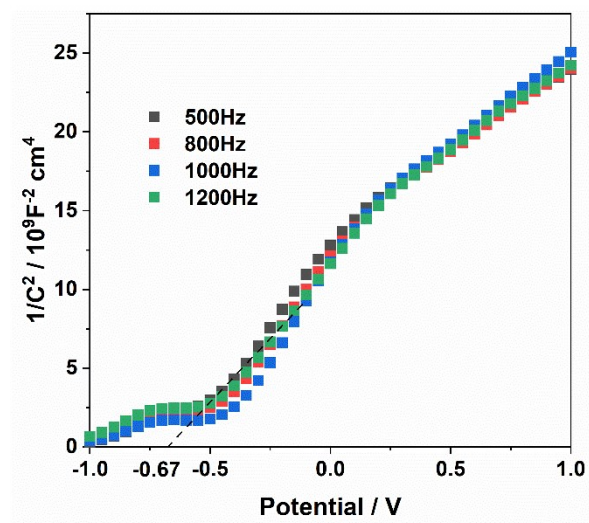


Figure S1 Mott-Schottky plots of W270-400 at 500Hz, 800 Hz, 1000 Hz and 1200.
Hz.

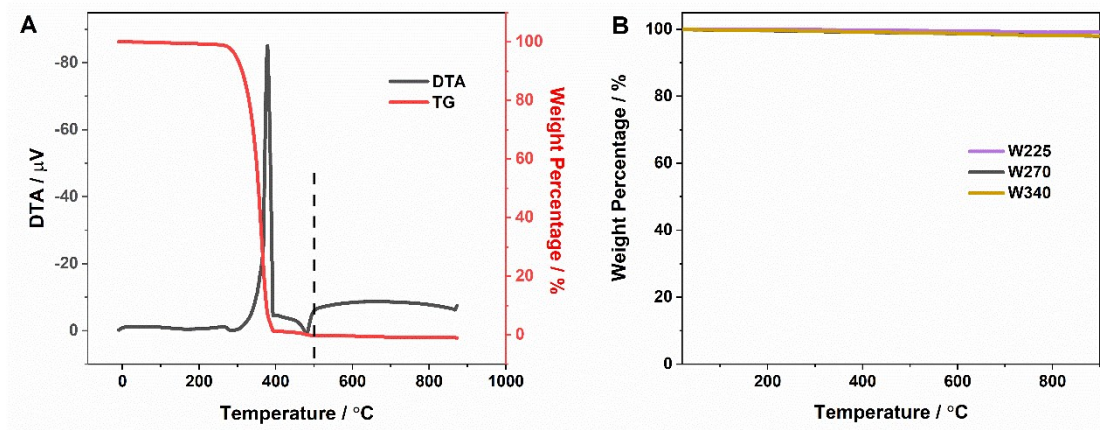


Figure S2 (A) The TG-DTA curves of P270 and (B) TG curves of W225, W270 and W340.

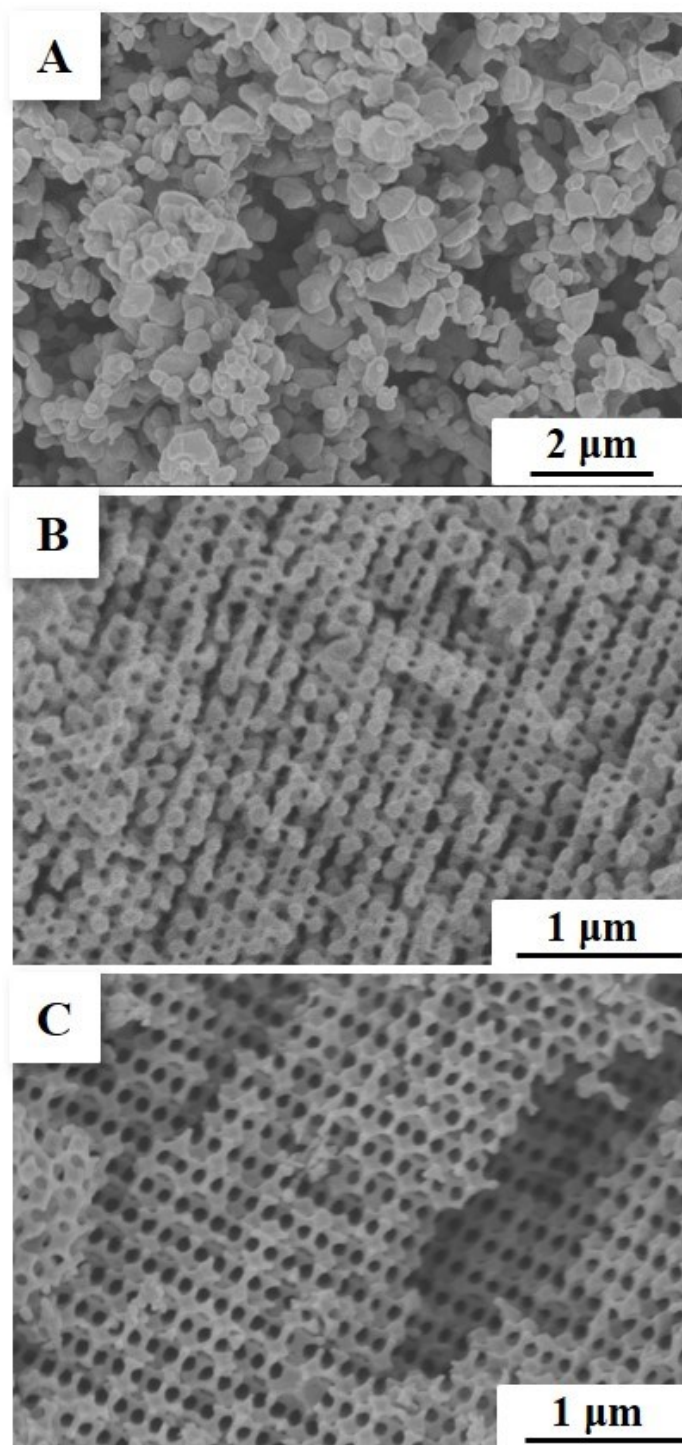


Figure S3 SEM images of W270 precursor calcined at different temperature. (A) 700 °C, (B) 600 °C and (C) 500 °C.

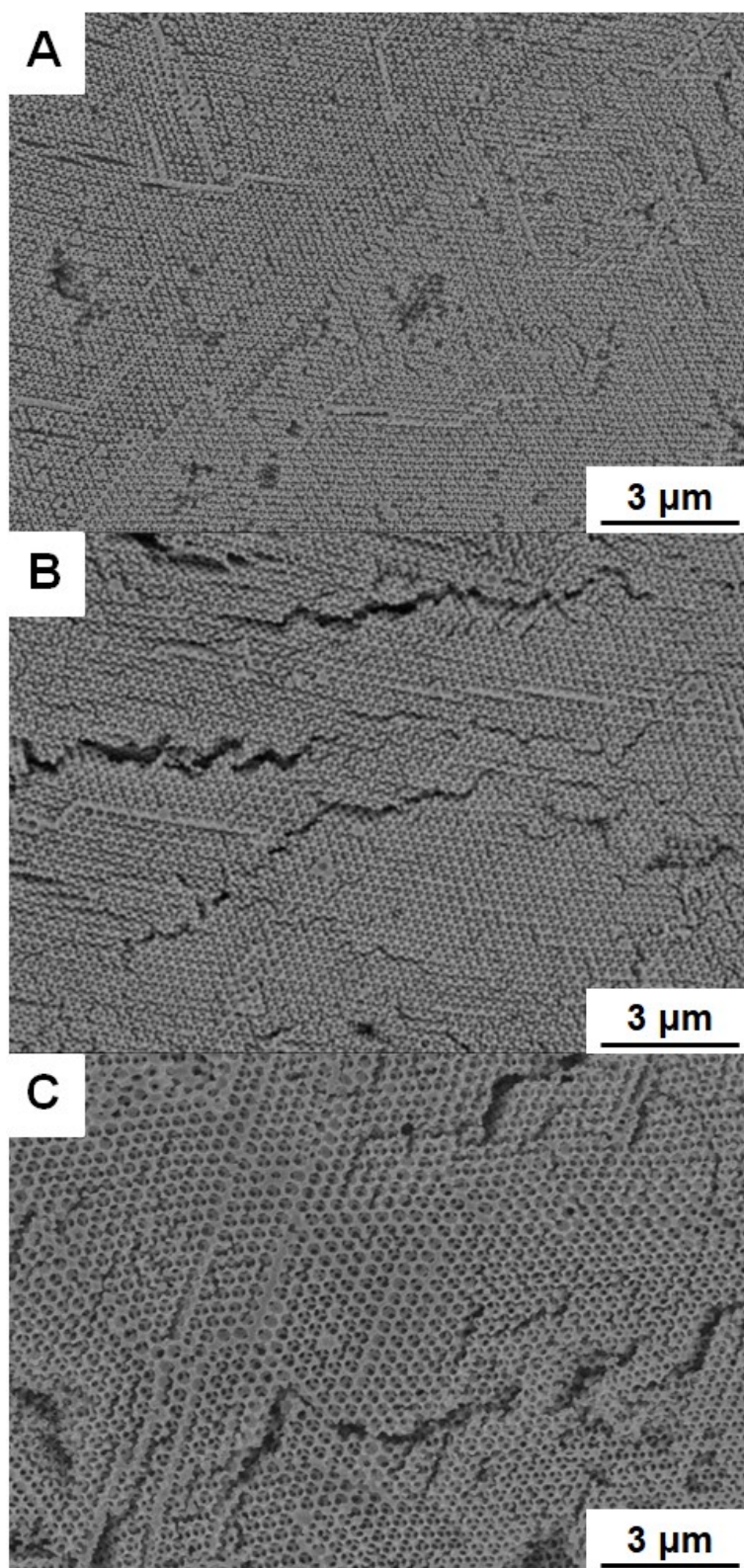


Figure S4 SEM images of (A) W225, (B) W270 and (C) W340.

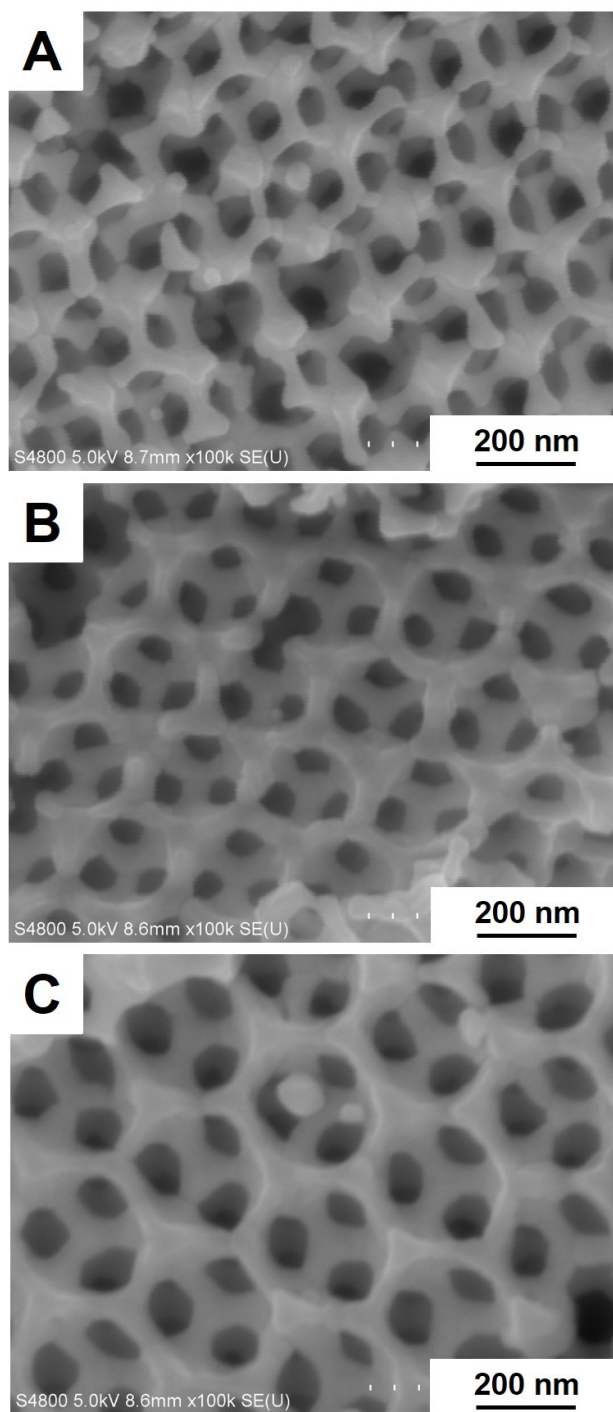


Figure S5 SEM images of (A) W225, (B) W270 and (C) W340 magnified 100k times.

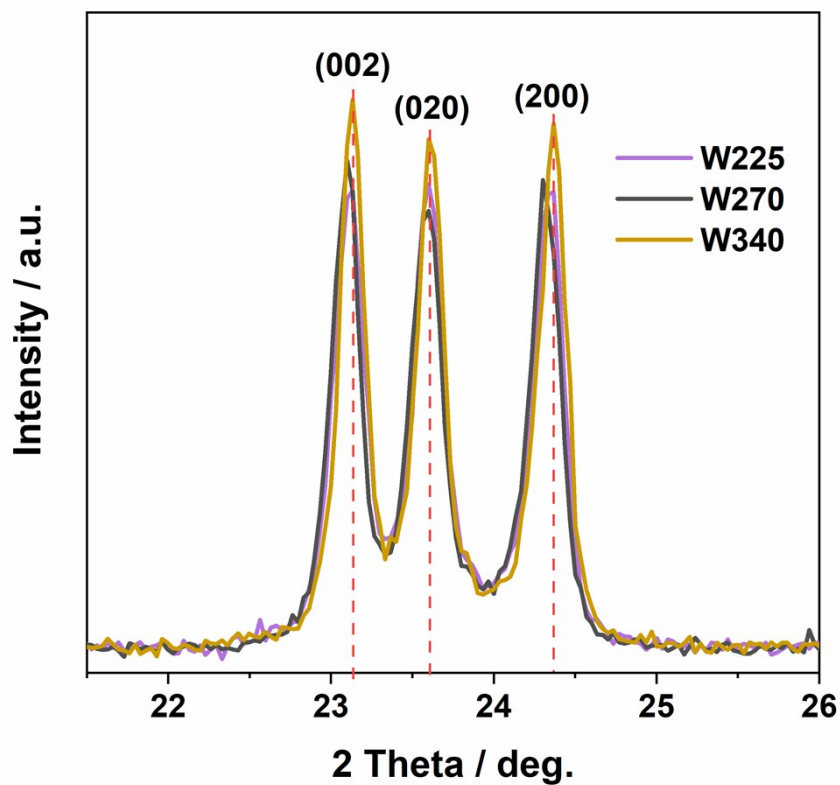


Figure S6 XRD patterns of W225, W270 and W340 ranged from 21.5 ° to 26 °.

The crystallite sizes of 3DOM WO₃ were calculated from the XRD results according to Scherrer's equation[6].

$$D = \frac{K\lambda}{\beta \cos\theta}$$

Where D is the mean size of the crystalline domains, λ is the X-ray wavelength, β is the full-width at half maximum, and θ is the Bragg diffraction angle.

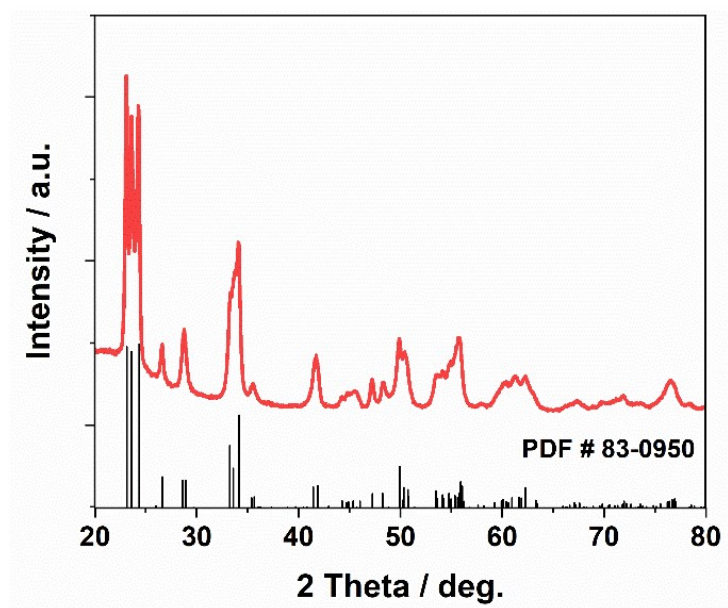


Figure S7 XRD patterns of WO₃ nanoparticles.

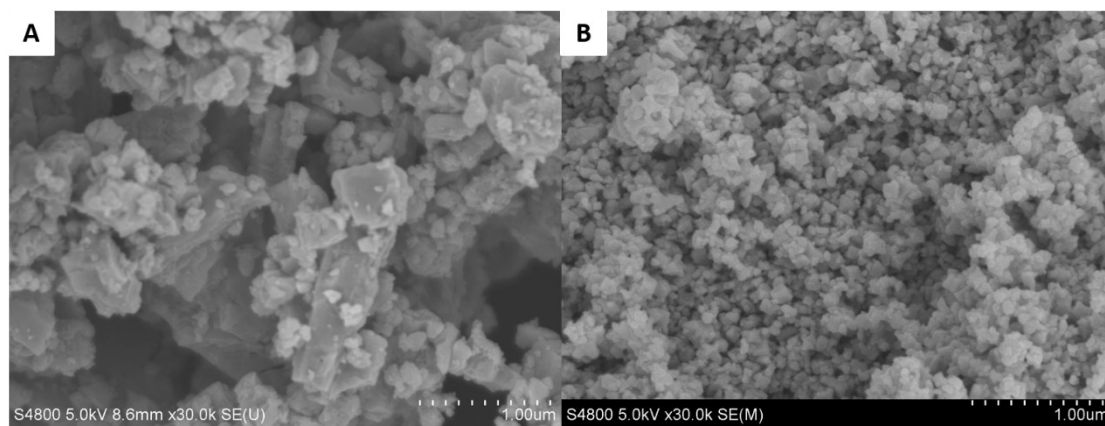


Figure S8 SEM image of (A) WO_3 nanoparticle, (B) W270-400-d.

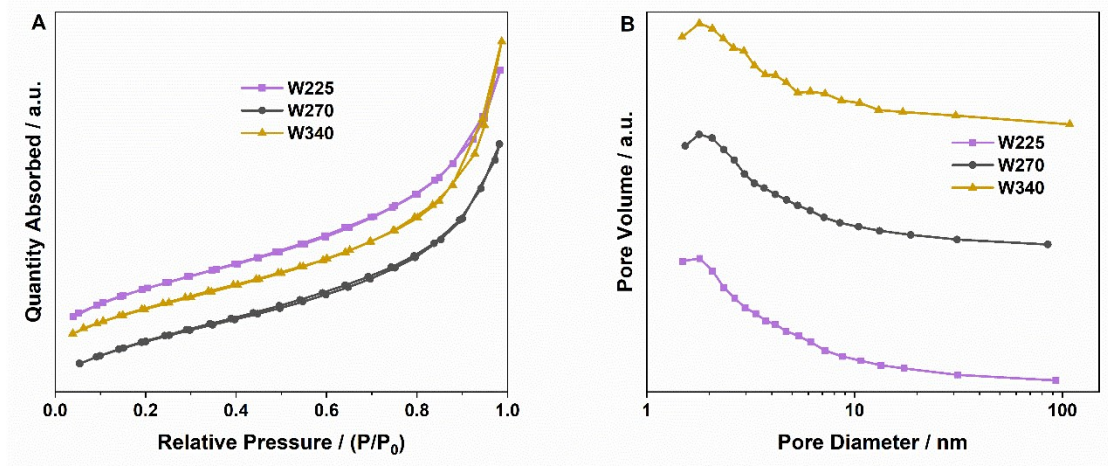


Figure S9 (A) Nitrogen adsorption-desorption isotherms and (B) corresponding pore size distribution curves of W225, W270 and W340.

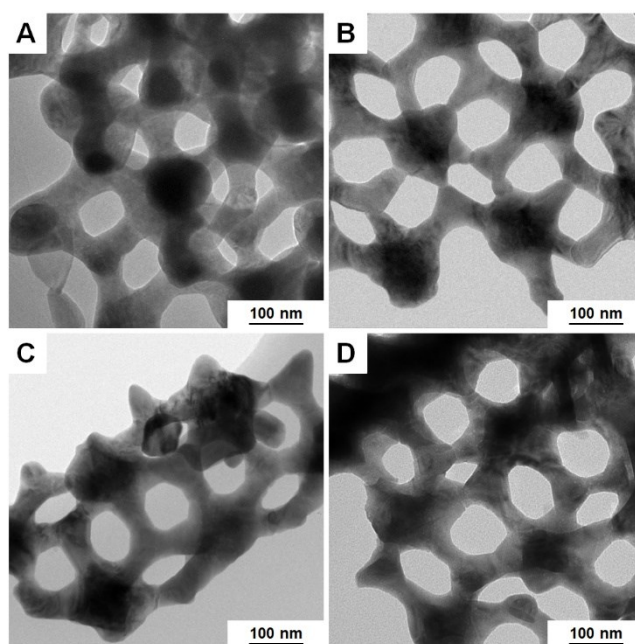


Figure S10 TEM images of (A) W270, (B) W270-300, (C) W270-400 and (D) W270-500.

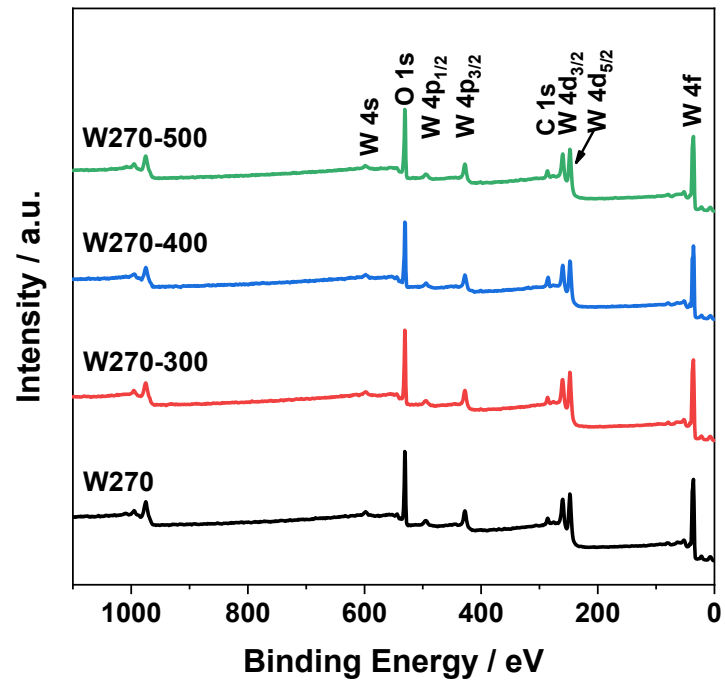


Figure S11 XPS survey spectra of W270, W270-300, W270-400 and W270-500.

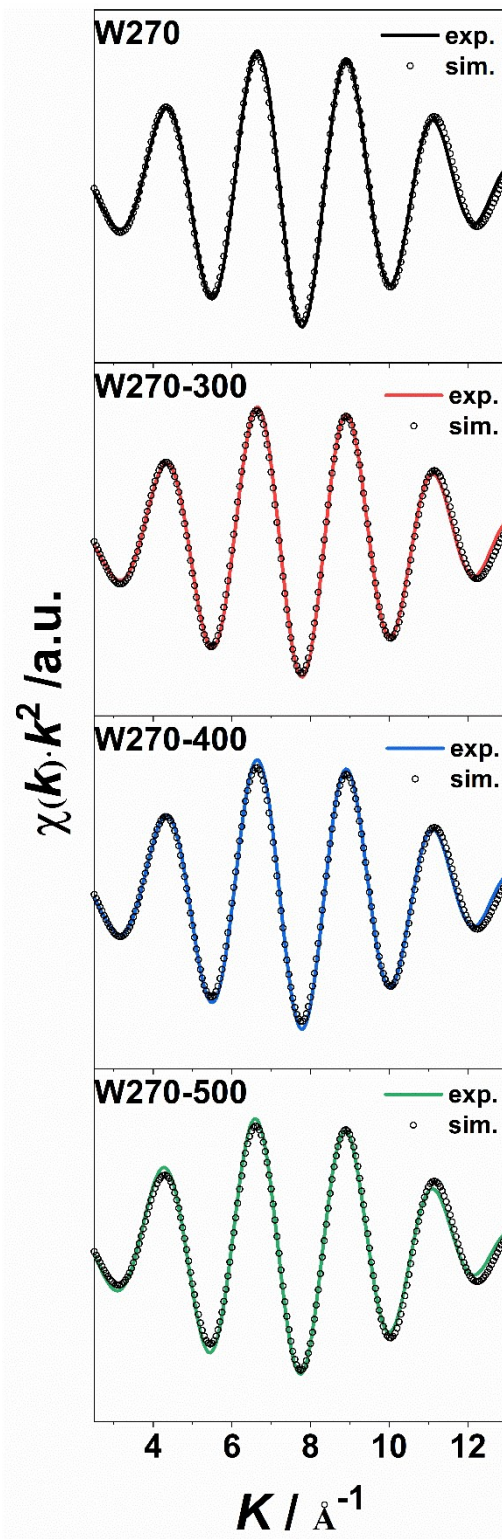


Figure S12 The Fourier transformation of filtered $k^2 \cdot \chi(k)$ in the k space of W270, W270-300, W270-400 and W270-500, the dotted lines corresponding to the fitting results.

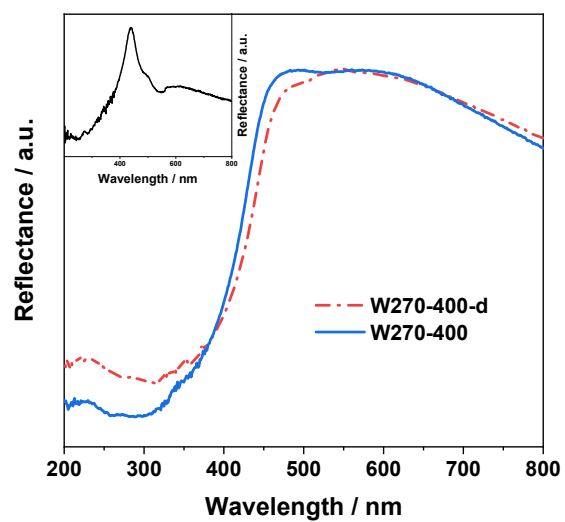


Figure S13 UV-vis diffuse reflectance spectra of W270-400 and W270-400-d, and the left insert is subtraction of the corresponding spectra.

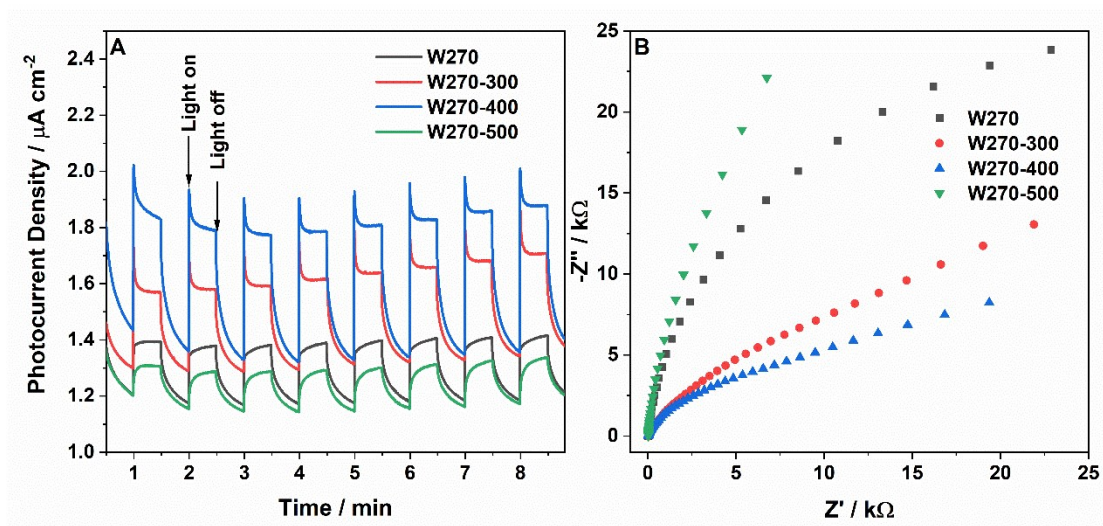


Figure S14 Photoelectrochemical properties of W270, W270-300, W270-400 and W270-500. (A) Photocurrent responses and (B) Nyquist plots of electrochemical impedance of the samples.

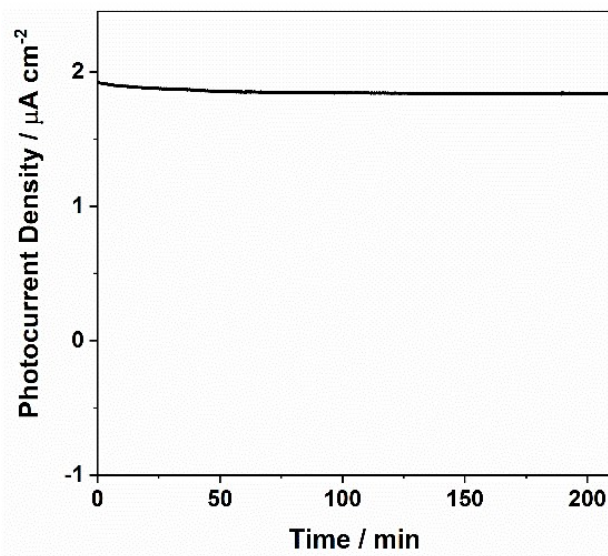


Figure S15 the long-term photocurrent of W270-400 obtained at 0.5 V Ag/AgCl.

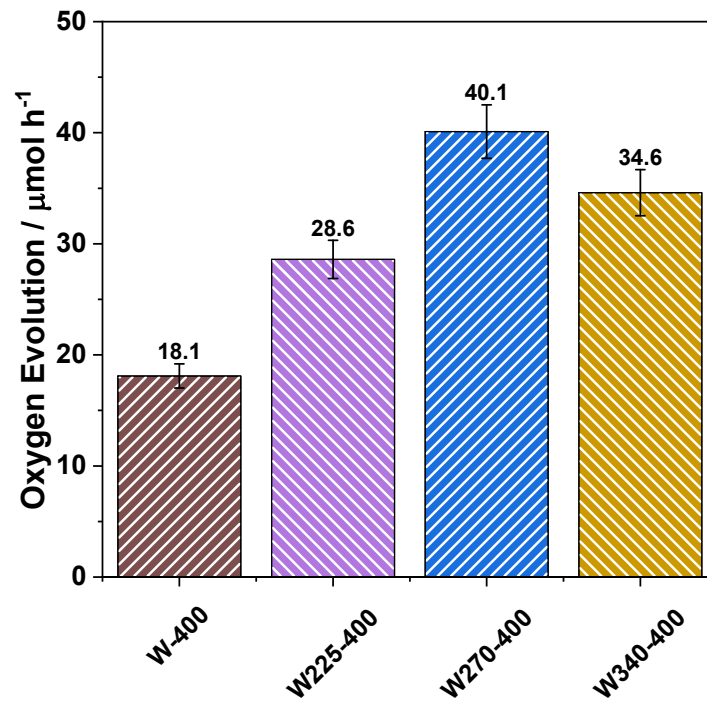


Figure S16 Photocatalytic O_2 evolution over the samples under the visible light irradiation ($\lambda > 400$ nm)

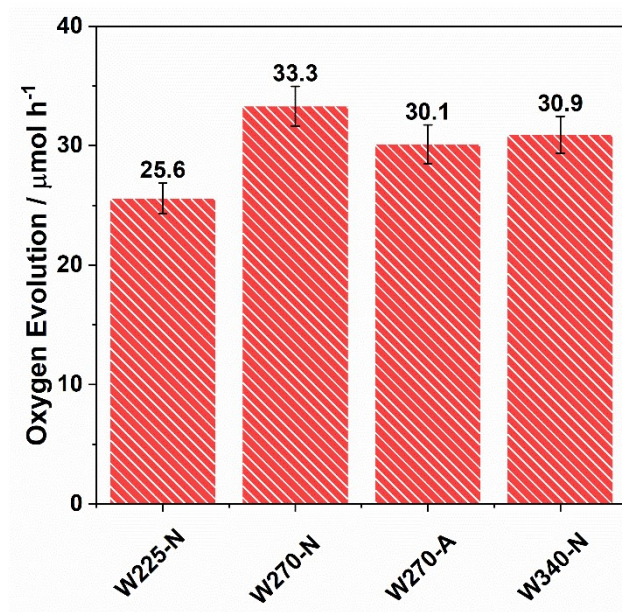


Figure S17 Photocatalytic O_2 evolution over the samples under the visible light irradiation ($\lambda > 400$ nm).

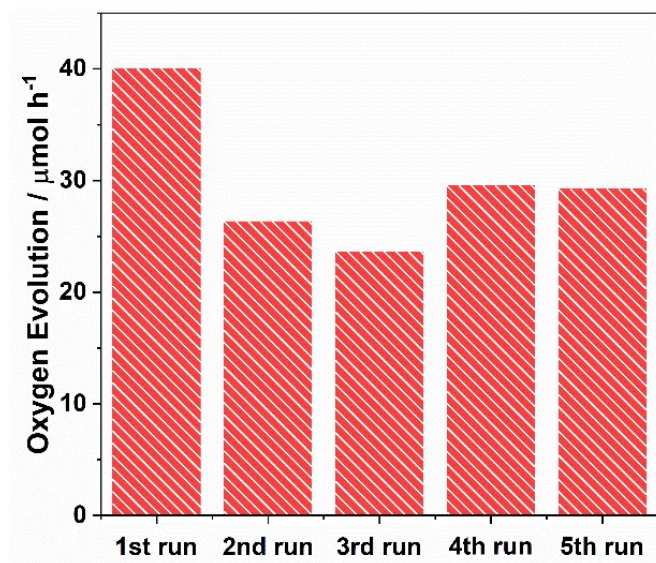


Figure S18 Recycle photocatalytic O_2 evolution over W270-400 under the visible light irradiation ($\lambda > 400 \text{ nm}$).

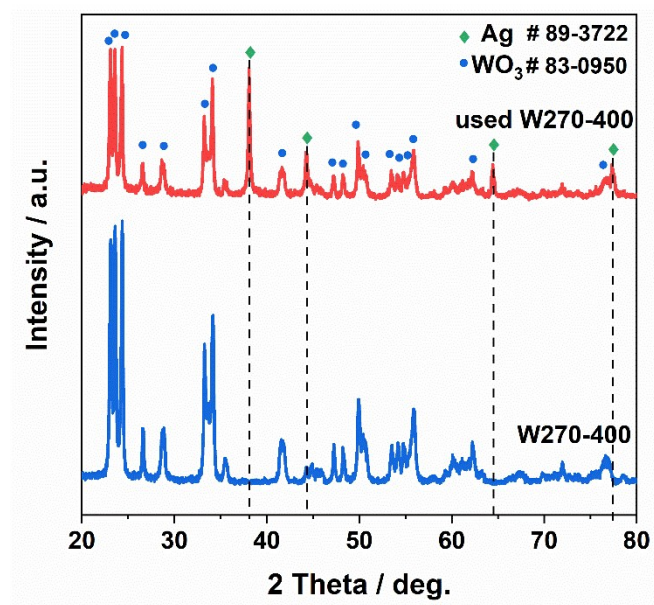


Figure S19 The XRD patterns of W270-400 and used W270-400

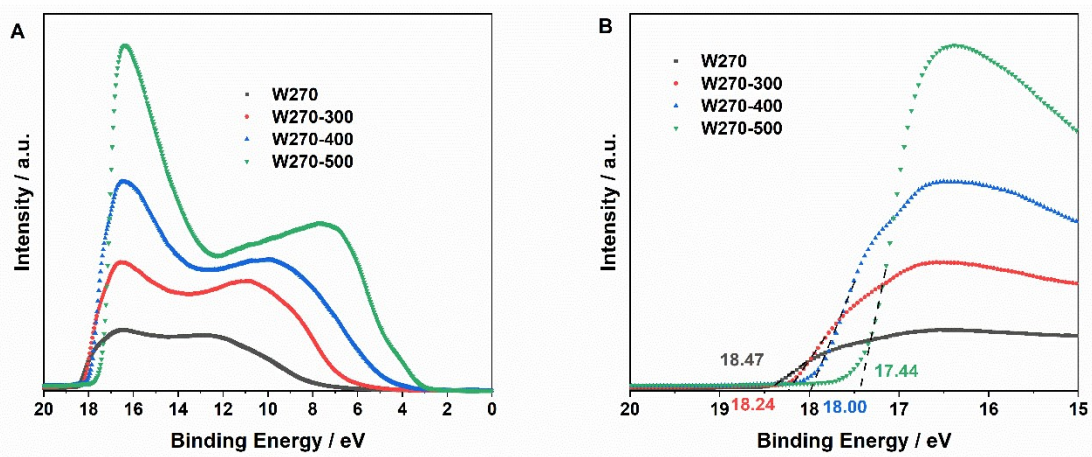


Figure S20 (A) Ultraviolet photoelectron spectra of W270, W270-300, W270-400 and W270-500, (B) partial magnification of (A).

Figure S20 shows the UPS of the samples. The Fermi energy (vs. vacuum level) of W270, W270-300, W270-400 and W270-500 are 2.75 eV, 2.98 eV, 3.22 eV and 3.78 eV, respectively. From the intercept on the abscissa of the Mott-Schottky plots and Nernst equation, the CBE of W270, W270-300, W270-400 and W270-500 are estimated to be 0.17, 0.23, 0.24 and 0.55 V vs NHE in Figure 10C. Because the energy difference between the bottom of the conduction band and the Fermi level is about 0.2, 0.3 and 0.4 eV for 10^2 , 10^3 and $> 10^4$ Ω cm in conductivity for oxide semiconductors, respectively [7], the estimated Fermi level values (vs. NHE) should follow the trends that $W270 < W270-300 < W270-400 < W270-500$.

3. Tables

Table S1 The reaction conditions of PS microspheres with different diameters

Reaction temperature (°C)	Volume of styrene (mL)	Diameter (nm)
98	15	225
88	15	270
88	24	340

Table S2 Physicochemical properties of W225, W270 and W340 measured by XRD and Raman.

Sample	Lattice parameters ^a			D (nm) ^a	FWHM (cm ⁻¹) ^b
	a (Å)	b (Å)	c (Å)		
W225	7.302	7.532	7.684	26.1	22.0
W270	7.308	7.534	7.697	26.3	22.0
W340	7.306	7.540	7.687	28.3	22.1

^a Determined by XRD

^b FWHM (full width at half maximum) of main Raman shifts (~ 806 cm⁻¹)

Table S3 The physicochemical properties of W225, W270 and W340.

samples	BET surface area (m ² /g)	Pore Diameter (nm)	Pore volume (cm ³ /g)
W225	8.884	1.799	0.009
W270	7.042	1.787	0.008
W340	7.325	1.794	0.010

PGB can be easily calculated according to the modified Bragg's law [8]:

$$\lambda = 2 \sqrt{\frac{2}{3}} D \sqrt{n_{\text{WO}_3}^2 f + n_{\text{void}}^2 (1 - f) - \sin^2 \theta}$$

where λ is the wavelength related to the PGB, D is the macropore size of each 3DOM WO_3 , n is the refractive index, f is the volume percentage of WO_3 and regularly taken as 0.26, and θ is the light incident angle. When the incident angle θ equals 0, the wavelength (λ) related to the PGB position is only dependent on the macropore size of 3DOM WO_3 . We calculated the PGB position and listed the results in Table S4. The PBG positions measured by reflectance spectra ($\lambda_{\text{measured}}$) and calculated by the modified Bragg's law ($\lambda_{\text{calculated}}$) are similar.

Table S4 The diameters of PS spheres, the pore diameter and the photonic stop band positions measured by reflectance spectra and calculated by the modified Bragg's law.

Samples	PS diameter (nm)	Pore diameter (nm)	Shrinkage (%)	$\lambda_{\text{measured}}$ (nm)	$\lambda_{\text{calculated}}$ (nm)
W225	225	169	25	-	355
W270	270	223	17	474	468
W340	340	269	21	570	565

Table S5 Binding energy (B.E.), relative peak area (P.A.) of O 1s, and the percentages of different surface oxygen species.

samples	B.E. of O 1s (eV)			P.A. (Counts)			Percentage (%)		
	O _L	O _{OH}	O _{ads}	O _L	O _{OH}	O _{ads}	O _L	O _{OH}	O _{ads}
W270	530.5	531.6	533.1	217922.1	45844.9	14558.8	78.3	16.5	5.2
W270-300	530.5	531.6	533.2	214947.6	45761.5	14332.5	78.2	16.6	5.2
W270-400	530.3	531.6	533.2	174625.1	57382.2	17190.6	70.0	23.0	7.0
W270-500	530.4	531.8	533.4	200684.0	49550.9	22988.4	73.5	18.1	8.4

Table S6 Binding energy (B.E.) and relative peak area (P.A.) of W 4f, and molar percentages (M.P.) of W⁵⁺ and W⁶⁺ species.

samples	B.E. (eV)				P.A. (Counts)		M.P. (%)	
	W ⁶⁺		W ⁵⁺		W ⁶⁺	W ⁵⁺	W ⁶⁺	W ⁵⁺
	4f _{5/2}	4f _{7/2}	4f _{5/2}	4f _{7/2}				
W270	37.8	35.7	-	-	374782.2	-	100	-
W270-300	37.8	35.7	36.8	34.7	363745.9	9552.96	97.4	2.6
W270-400	37.7	35.5	36.7	34.5	287178.0	23618.44	92.4	7.6
W270-500	37.7	36.6	36.7	34.6	316073.6	22821.17	93.3	6.7

Table S7 TON, TOF and AQE of the as-prepared samples.

Samples	TOF (h ⁻¹)	TON	AQE (%)
W270	0.55	0.55	2.77
W270-300	0.56	0.56	2.89
W270-400	0.74	0.74	3.73
W270-500	0.37	0.37	1.84

In Figure 10C, from the intercept on the abscissa, the flat band potentials of W270, W270-300, W270-400 and W270-500 were estimated to be -0.74, -0.68, -0.67 and -0.36 V versus Ag/AgCl. The potential measured relative to the Ag/AgCl reference can be converted into normal hydrogen electrode (NHE) potential according to the following equation.

$$E_{\text{fb}}(\text{vs NHE}) = E_{\text{fb}}(\text{pH}=0, \text{vs Ag/AgCl}) + E_{\text{AgCl}} + 0.059 \times \text{pH}$$

where $E_{\text{AgCl}} = 0.197$ V, and the pH value of the electrolyte is measured to be 14. For the undoped n-type semiconductors, the conduction band edge (CBE) is 0.1-0.3 V higher than that of E_{fb} .

4. References

- [1] X. Zou, Y. Dong, J. Ke, H. Ge, D. Chen, H. Sun, Y. Cui, Cobalt monoxide/tungsten trioxide p-n heterojunction boosting charge separation for efficient visible-light-driven gaseous toluene degradation, *Chem. Eng. J.*, 400 (2020) 125919.
- [2] Y. Liu, B.R. Wygant, K. Kawashima, O. Mabayoje, T.E. Hong, S.-G. Lee, J. Lin, J.-H. Kim, K. Yubuta, W. Li, J. Li, C.B. Mullins, Facet effect on the photoelectrochemical performance of a $\text{WO}_3/\text{BiVO}_4$ heterojunction photoanode, *Appl. Catal. B: Environ.*, 245 (2019) 227-239.
- [3] Y. Sasaki, A. Iwase, H. Kato, A. Kudo, The effect of co-catalyst for Z-scheme photocatalysis systems with an $\text{Fe}^{3+}/\text{Fe}^{2+}$ electron mediator on overall water splitting under visible light irradiation, *J. Catal.*, 259 (2008) 133-137.
- [4] L. Qin, R. Ru, J. Mao, Q. Meng, Z. Fan, X. Li, G. Zhang, Assembly of MOFs/polymer hydrogel derived $\text{Fe}_3\text{O}_4\text{-CuO}@$ hollow carbon spheres for photochemical oxidation: Freezing replacement for structural adjustment, *Appl. Catal. B: Environ.*, 269 (2020) 118754.
- [5] Y. Wang, J. Cai, M. Wu, J. Chen, W. Zhao, Y. Tian, T. Ding, J. Zhang, Z. Jiang, X. Li, Rational construction of oxygen vacancies onto tungsten trioxide to improve visible light photocatalytic water oxidation reaction, *Appl. Catal. B: Environ.*, 239 (2018) 398-407.
- [6] F. Gu, C. Luo, D. Han, S. Hong, Z. Wang, Atomically dispersed Pt on 3DOM WO_3 promoted with cobalt and nickel oxides for highly selective and highly sensitive detection of xylene, *Sens. Actuators B Chem.*, 297 (2019) 126772.

[7] U.K. Kirner, K.D. Schierbaum, W. Göpel, Interface-reactions of Pt/TiO₂: Comparative electrical, XPS-, and AES-depth profile investigations, *Fresen. J. Anal. Chem.*, 341 (1991) 416-420.

[8] J. Cai, M. Wu, Y. Wang, H. Zhang, M. Meng, Y. Tian, X. Li, J. Zhang, L. Zheng, J. Gong, Synergetic Enhancement of Light Harvesting and Charge Separation over Surface-Disorder-Engineered TiO₂ Photonic Crystals, *Chem*, 2 (2017) 877-892.